2018 European Control Conference (ECC)
June 12-15, 2018. Limassol, Cyprus

Robust control of a tethered kite for ship propulsion

Baptiste Cadalen[1,2], Patrick Lanusse[1], Jocelyn Sabatier[1], Fabien Griffon[2] and Yves Parlier[2]

***Abstract*— Airborne Wind Energy (AWE) systems are among the most promising technologies in terms of clean and green energy. They present an innovative solution to harvest energy from higher altitudes than traditional wind turbines by replacing expensive towers with lightweight tethers. One application of an AWE system is using the traction force of a fast-flying airfoil, or kite, for ship propulsion. This paper considers the design of an automatic pilot capable of generating a sufficient traction force by steering a kite on a desired trajectory. The design requires a kite model, as well as a path-following strategy. Then, a robust controller is proposed to ensure the stability of the system with respect to all the uncertainties that arise in such a complex environment.**

I. INTRODUCTION

The need to reduce CO_2 emissions and the increase in oil prices affect all transportation industries and especially the maritime industry. This has fostered interest in designing energy-saving propulsion systems for ships. Taking advantage of wind energy by using tethered airfoils, or kites, as an alternative or complementary propulsion source can be an effective solution [16]. It involves an AWE (Airborne Wind Energy) concept, operating at high altitudes, where the wind is stronger and steadier. AWE concepts can be used to convert the traction power of tethered airfoils into electricity effectively [13], [6] or into ship propulsion, as is the case of the *Beyond The Sea* project [22].

In order to achieve a wind propulsion system for ships, a towing kite following a dynamic trajectory is the most interesting candidate for such a purpose [15], [24]. In contrast to a static flight, the dynamic motion of a tethered wing with an eight-shaped pattern can provide sufficient energy through traction to tow a ship. The advantages are an endless source of energy from the wind, as well as a compact, light-weight system that can be used or put away easily, taking up very little space.

The intention of the *Beyond The Sea* project is to develop an automatic pilot which can steer a kite into a predetermined eight-shaped trajectory and manage rapidly changing conditions outside, especially changes in the wind speed. A global overview of this system is shown in Fig. 1. In this paper, the focus is first on modelling a tethered wing which can be used to design a robust controller. Section 2 provides a strategy for the kite to follow a designated figure-of-eight pattern. Then, section 3 deals with the design of a robust control law to ensure the stability of the closed loop. Finally, this paper reports simulation results of the implemented system and concludes with remarks on the proper functioning of the controller.

II. KITE MODELLING

A. Context & assumptions

This section aims at delivering a suitable model for controlling a kite on a defined trajectory. Several models have been proposed in the literature. Each tries to replicate the dynamic motion of a kite, from low complexity models to very detailed ones. A zero mass model such as those in [7], [3] and [15], is not entirely suited for robust control because of its low complexity and accuracy, whereas the most advanced models taking into account the mechanics of deformable solids or multi-body systems [1], [5], [4] are too resource consuming and excessively complex for control. However, inspired by several models proposed in [8], [21] or [11], a combined point-mass and rigid-body model was developed in this paper, as it offers the simplicity of a point-mass model, while integrating the kite angular velocity as well.

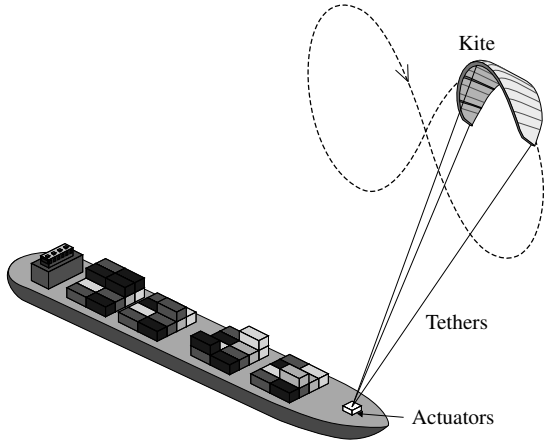

Fig. 1. Representation of kite automatic pilot for ship propulsion

B. Coordinate references

The model described in this paper is based on several coordinate systems. As shown in Fig. 2, the main coordinate reference $\mathrm{R_{WR}} = (\mathrm{O},\ \mathbf{x}_{\mathrm{WR}},\ \mathbf{y}_{\mathrm{WR}},\ \mathbf{z}_{\mathrm{WR}})$ is attached to the anchor point of the ship O and directed along the relative wind of the ship by its unit vector $\mathbf{x}_{\mathrm{WR}}$. The $\mathbf{z}_{\mathrm{WR}}$ axis points downwards with respect to gravity. The relative wind of the ship is the wind perceived by standing on the moving vessel. The kite position is associated to the $\mathrm{R_{k0}} = (\mathrm{K},\ \mathbf{x}_{\mathrm{k0}},\ \mathbf{y}_{\mathrm{k0}},\ \mathbf{z}_{\mathrm{k0}})$ reference frame, and the kite attitude is described by the $\mathrm{R_b} = (\mathrm{K},\ \mathbf{x}_{\mathrm{b}},\ \mathbf{y}_{\mathrm{b}},\ \mathbf{z}_{\mathrm{b}})$ reference frame. Both reference frames are centered at the kite position, noted K, as illustrated in Fig. 2.

By applying Newton's second law of motion to the kite in the reference frame $\mathrm{R_{k0}}$, the elevation and azimuth accelerations can be computed by the following equations:

$$\ddot{\theta} = \frac{-\mathbf{F}.\mathbf{x}_{\mathrm{k0}}}{rm} - \sin(\theta)\cos(\theta)\dot{\phi}^2 \tag{1}$$

$$\ddot{\phi} = \frac{\mathbf{F}.\mathbf{y}_{\mathrm{k0}}}{rm\cos(\theta)} - 2\tan(\theta)\dot{\theta}\dot{\phi}, \tag{2}$$

where m is the kite mass and r is the tether length. Here, $\mathbf{F}$ denotes the sum of all the forces applied at the kite centre of mass K, with respect to $\mathrm{R_{k0}}$. This global force

[1] IMS, Univ. Bordeaux, 351 cours de la liberation, 33405 Talence cedex, France {firstname.lastname}@ims-bordeaux.fr
[2] Beyond The Sea, 1010 Avenue de l'Europe, 33260 La Teste de Buch firstname.lastname@beyond-the-sea.com

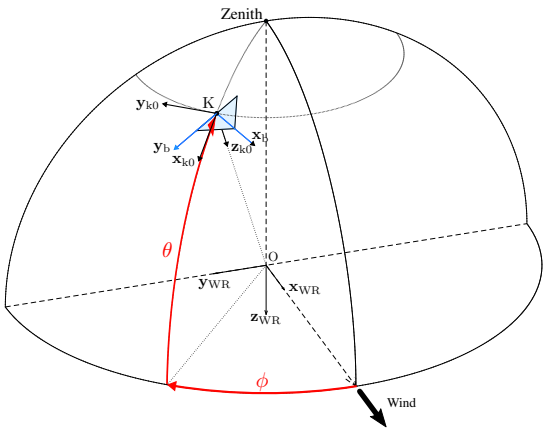

Fig. 2. Wind window and reference frames. θ represents the elevation of the kite while ϕ is the azimuth

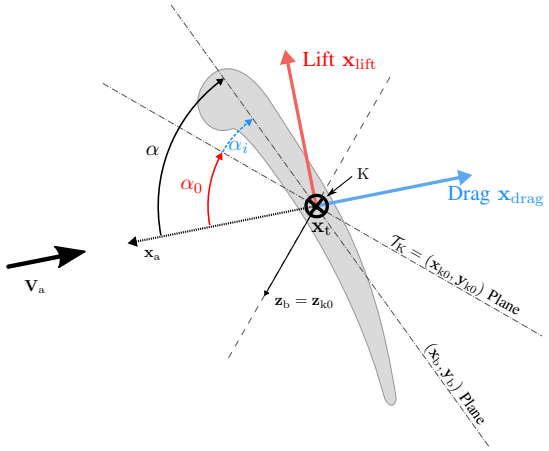

Fig. 3. Aerodynamic forces applied to the kite, at point K

is composed of all the aerodynamic forces labelled $\mathbf{F}_a$, as well as the gravitational force $\mathbf{F}_g$:

$$\mathbf{F} = \mathbf{F}_a + \mathbf{F}_g. \tag{3}$$

C. Aerodynamic forces

The aerodynamic forces $\mathbf{F}_a$ depend mainly on the apparent wind velocity vector $\mathbf{V}_a$ seen by the kite. As usual in aerodynamics, the apparent wind is calculated by the expression $\mathbf{V}_a = \mathbf{V}_{WR} - \mathbf{V}_k$. By definition, the drag force has the same direction as the apparent wind seen by the kite, as shown in Fig. 3. The lift is perpendicular to the drag and to the transverse axis $\mathbf{y}_b$ of the kite. The transverse aerodynamic force is along the kite transverse axis. As explained in [2], the combination of all the aerodynamic forces yields :

$$\begin{aligned}\mathbf{F}_a = \frac{1}{2}\rho C_L A_k |\mathbf{V}_a|^2 \mathbf{x}_{lift} + \frac{1}{2}\rho C_D A_k |\mathbf{V}_a|^2 \mathbf{x}_{drag} + \\ \frac{1}{2}\rho C_t A_k |\mathbf{V}_a|^2 \mathbf{x}_t.\end{aligned} \tag{4}$$

D. Turn rate law

As opposed to a symmetrical steering input, the influence of a differential, or asymmetrical, steering for the kite is essentially related to its angular velocity. Indeed, the calculation of the kite's angular rate when applying a steering input shows that the parameter which is the most influenced by the input is the yaw rate. The others will be neglected as their contributions are sufficiently small compared to the yaw rate. An empirical equation discussed in other studies [7], [11] and [9] is proposed to account for this behaviour. The dynamic response to a steering input δ is thus modelled by the following equation:

$$\dot{\psi} = g_k v_a \delta + M \frac{\cos\theta \sin\psi}{v_a} - \phi \sin\theta. \tag{5}$$

where v_a is the airflow projected on the $\mathbf{x}_b$ axis and g_k is a constant parameter, specific to each kite, that must be deduced from real measurements. As explained in [7] the second term of (5) accounts for the effect of mass distribution in the kite, M being another constant to determine.

E. State space representation

Using (1), (2), (3) and (5), the model can be written as a nonlinear state space representation with 5 states. The input U is a vector with the asymmetrical steering input δ and the symmetrical steering input ϵ :

$$\begin{cases}\dot{X}(t) = f(X(t), U(t)) \\ Y(t) = g(X(t), U(t))\end{cases} \quad \text{with } X = \begin{bmatrix}\theta \\ \phi \\ \dot{\theta} \\ \dot{\phi} \\ \dot{\psi}\end{bmatrix} \quad U = \begin{bmatrix}\delta \\ \epsilon\end{bmatrix}. \tag{6}$$

f is a nonlinear function, gathering (1), (2), (3) and (5) that describes the evolution of the system state X, while g is the output function. The following model parameters still need to be known before a simulation: g_k, M, C_D, C_L and C_t. They depend on the kite wing itself, and need to be determined by experimental tests as explained in the next section.

III. PATH-FOLLOWING STRATEGY

As seen in the introduction, the main purpose of the autopilot is to ensure that the kite follows an eight-shaped path within the wind window. The strategy proposed here consists in following a predetermined path, sampled in an certain number of points, and periodic to create an infinite path. The kite will then follow each point in successive order to achieve the following behaviour. The trajectory shown in Fig. 4 can be defined by its azimuth and elevation with the parameter s:

$$\begin{cases}\phi = \phi_0 + \Delta\phi \frac{\sin s}{1+\cos^2 s} \\ \theta = \theta_0 + \Delta\theta \frac{\sin s \cos s}{1+\cos^2 s}\end{cases} \quad s \in [0, 2\pi]. \tag{7}$$

Equation (7) suggests that the trajectory is not a function of time. Therefore, following the path does not depend on time but on space. The trajectory is thus spatially sampled in a series of points P_i, evaluated in the R_{WR} reference frame. The strategy resides in determining the best point P_i the kite should follow at a given time, denoted as P. This point P

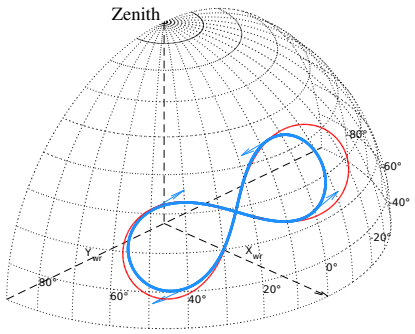

Fig. 4. Example of an arbitrary eight-shaped trajectory, on the tangent plane $\mathcal{T}_{(\theta_0,\phi_0)}$ (red) and projected on the wind window (blue)

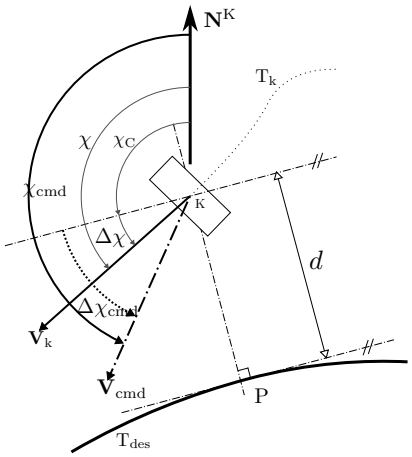

Fig. 5. Desired kite velocity to reach and follow $\mathrm{T_{des}}$

also changes relative to the kite position. For more detail on this algorithm see [2].

A. Desired Orientation

The trajectory's optimal point has been calculated but its desired orientation angle also needs to be computed. To follow the trajectory, a desired velocity can be deduced from Fig. 5 which will ensure that the kite travels towards and along the trajectory. To control the kite motion, its velocity vector is used, characterized by its χ angle. Therefore, the desired orientation angle is a combination of the trajectory orientation χ_{C} and a chosen orientation χ_{cmd}:

$$\chi_{\mathrm{cmd}} = \chi_{\mathrm{C}} + \Delta\chi_{\mathrm{cmd}}(d). \tag{8}$$

χ_{C} represents the trajectory orientation. $\Delta\chi_{\mathrm{cmd}}(d)$ is the chosen orientation, which is calculated while taking the error distance d into account. By observing Fig. 5, $\Delta\chi_{\mathrm{cmd}}(d)$ can either make the kite align with the tangent to the trajectory, or make the kite point directly towards the trajectory. However, the desired behaviour of the path-following algorithm is that the further away the kite is, the more direct its direction towards the trajectory should be, equivalent to $\Delta\chi_{\mathrm{cmd}} \to \frac{\pi}{2}$. If the kite is already close to the trajectory, then it should align itself with the tangent vector at point P, by imposing $\Delta\chi_{\mathrm{cmd}} \to 0$. This behaviour can be achieved by the following relation:

$$\Delta\chi_{\mathrm{cmd}}(d) = \arctan\left(\frac{d}{d_0}\right), \tag{9}$$

where d_0 is a pivot point. This distance is the point where the kite is pointing equally towards and along the desired trajectory, i.e $\Delta\chi_{\mathrm{cmd}} = 45°$.

IV. Robust Controller

The purpose of the closed loop shown in Fig. 6 is to steer the kite so that its velocity vector reaches the desired velocity calculated by the path-following strategy. The error angle between the two is calculated as ϵ_χ by the relation:

$$\epsilon_\chi = \chi - \chi_{\mathrm{cmd}}. \tag{10}$$

The instability of the kite in open loop means that a closed loop identification has to be used. It is thus necessary to conduct the identification under feedback by first implementing a proportional controller for $C(s)$ to ensure stability of the closed loop. The gain was chosen sufficiently high so that the closed loop does not attenuate the identification

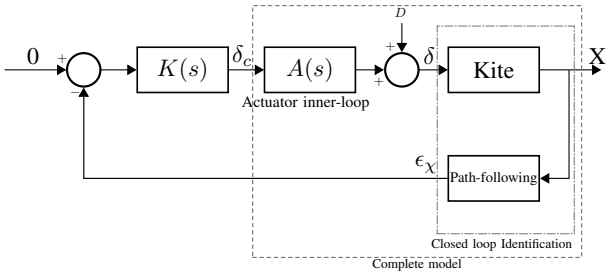

Fig. 6. Closed loop system composed of the kite itself, the path-following strategy and the actuators. The robust controller is represented by $K(s)$.

around the kite cutoff frequency, but not too high so that the added disturbance D can still be seen by the system. The model being identified is composed of the kite itself and the path-following block. The actuators were not included in the model during the identification process.

The input of the model is the asymmetrical input δ. Slacking and hauling were neglected in these simulations, meaning that the $(\mathbf{x}_\mathrm{b}, \mathbf{y}_\mathrm{b})$ plane is considered to always be tangent to the wind window. The output is then the error angle ϵ_χ. The actuators used by Beyond The Sea are then modelled and complete the entire set of models.

A. Closed loop identification

Because the combined nonlinear model of the kite and path-following strategy is highly nonlinear, it is then linearised around given eight-shaped trajectories using a closed loop identification. Experimental data are not used to identify the linear model as experimental tests can be time consuming and desired wind conditions are often difficult to find. Moreover, the methodology presented here is to be applicable to every kite desired and not only the one used in this example. Therefore, the model described before enables a efficient linearisation of a kite with different size or other parameters. Initially, a wind velocity and specific trajectory are chosen to identify the model. To make a frequency domain analysis of the system, a sinusoidal disturbance D is added to the input δ, with a frequency varying within a given range and applied to the model. Filtering the input and output signal of the system, a module and phase can be calculated for each frequency. From these frequency data, a model can then be fitted from all the simulations. A new wind velocity or another trajectory can be chosen and the same process can be applied. In this paper, the models are obtained for

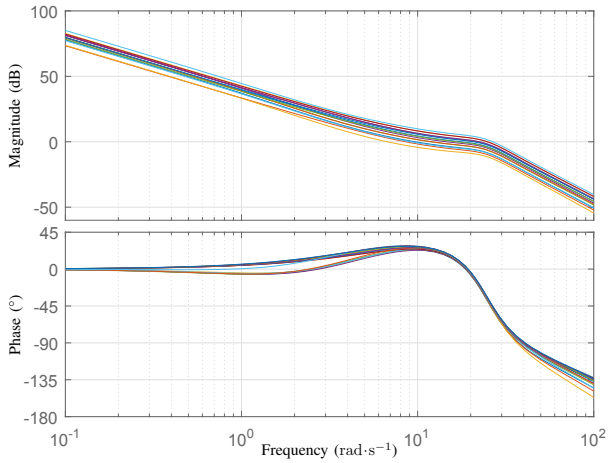

Fig. 7. Bode diagrams of the transfer function linking the command δ to the error angle ϵ_χ for different wind conditions and trajectories.

wind velocities ranging from $20\,\mathrm{km\cdot h^{-1}}$ to $60\,\mathrm{km\cdot h^{-1}}$. The trajectory parameters, such as the position, size or rotation were also changed. Three different trajectories were considered. The first one is a horizontal and centered trajectory. The second is similar but rotated around its centre. The third one is shifted and rotated within the wind window, so as to realise an arbitrary trajectory. Each of the trajectories was simulated with different wind conditions, giving five models for each trajectory. The nonlinear behaviour of the system is thus taken into account in a family of 15 linear frequency responses.

B. Actuators

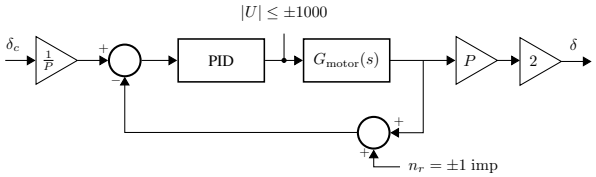

Fig. 8. Actuator inner loop $A(s)$. The gain 2 at the end accounts for the two motors acting in parallel. n_r models the shaft encoder noise and P is the encoder pulse to tether length conversion gain.

The command of the kite δ is achieved by two electrical motors, considered identical, which can reel in or out the two command lines. While not elaborated in this paper, an identification of one rotor yields an order two transfer function $G_{\mathrm{motor}}(s)$, defined by

$$G_{\mathrm{motor}}(s) = \frac{\mathrm{K_{motor}}}{s\left(1+\frac{s}{\omega_c^r}\right)}, \tag{11}$$

where $\mathrm{K_{motor}}$ is the static gain of the model, and ω_c^r the rotor cutoff frequency. Combining the two motors forms the $A(s)$ inner-loop which also involves a PID controller. This loop is represented in Fig. 8 where the output is the command δ applied to the tethers. The control input U of each actuator is limited by ± 1000. Therefore, the maximum speed of the tether command δ is $0.50\,\mathrm{m\cdot s^{-1}}$. The 15 final parametric models of the system including the motors dynamic are shown in Fig. 7. Then, this model set can be used to design a robust controller.

C. CRONE Control Design Methodology

Based on the frequency responses obtained, a robust Crone controller is then proposed to account for the nonlinear behaviour of the system and actuator dynamics. The wind and the trajectory itself are parameters that can cause uncertainties on the model as well.

The CRONE control-system design methodology is a frequency-domain approach developed since the eighties ([17], [18], [19], [23], [20]). It is based on the common unity-feedback configuration. Considering the robustness/performance-quality trade-off, with CRONE control, the plant uncertainties are taken into account by using structured frequency uncertainty domains. This allows least-conservative control systems unlike H_∞ designs. As a result, better performances can be obtained as shown in [19], [12]. The principle of the third generation CRONE control methodology is to optimize the parameter of a nominal open-loop transfer function $\beta_0(s)$ that includes a band-limited complex fractional order integration:

$$\beta_0(s) = \beta_l(s)\beta_m(s)\beta_h(s), \tag{12}$$

- where $\beta_m(s)$ is a set of complex order integrators:

$$\beta_m(s) = \prod_{k=-N^-}^{N^+} \beta_{m_k}(s), \tag{13}$$

with

$$\begin{aligned}\beta_{m_k}(s) \quad = \quad & C_k^{\mathrm{sign}(b_k)}\left(\alpha_k \tfrac{1+s/\omega_{k+1}}{1+s/\omega_k}\right)^{a_k} \\ & \left(\Re e_{/i}\left\{\left(\alpha_k \tfrac{1+s/\omega_{k+1}}{1+s/\omega_k}\right)^{\mathrm{i}b_k}\right\}\right)^{-q_k \mathrm{sign}(b_k)} \\ & \text{with} \\ & \alpha_k = (\omega_{k+1}/\omega_k)^{1/2} \text{ for } k \neq 0 \\ & \alpha_0 = \left(1+\left(\tfrac{\omega_r}{\omega_0}\right)^2 \Big/ 1+\left(\tfrac{\omega_r}{\omega_1}\right)^2\right)^{1/2}\end{aligned} \tag{14}$$

- where $\beta_l(s)$ is an integer order n_l proportional integrator and where $\beta_h(s)$ is a low-pass filter of integer order n_h:

$$\beta_l(s) = C_l\left(\frac{\omega_{-N^-}}{s}+1\right)^{n_l},\ \beta_h(s) = C_h\left(\frac{s}{\omega_{N^+}}+1\right)^{-n_h}. \tag{15}$$

Gains C_k, C_l and C_h are such that ω_r is the closed-loop resonant frequency. Order n_l has to be set to manage the accuracy provided by the control-system. Order n_h has to be set to obtain a proper or bi-proper control. When it is useful, N^- and N^+ are different from 0 to increase the number of tuning parameters.

The open loop parameters are optimized in order to reduce the variation of the resonant peak M_T of the complementary sensitivity function $T(s)$. The following robustness cost function can be minimized:

$$J = \left(M_{T0} - \inf_G |M_T|\right)^2 + \left(\sup_G |M_T| - M_{T0}\right)^2, \tag{16}$$

where M_{T0} is a required value of the nominal closed loop resonant peak (for the nominal plant G_0), while respecting the following set of inequality constraints for all plants G and for $\omega \in \mathbb{R}^+$:

$$\begin{aligned}&\inf_G |T(\mathrm{j}\omega)| \geq T_l(\omega), \qquad \sup_G |T(\mathrm{j}\omega)| \leq T_u(\omega), \\ &\sup_G |S(\mathrm{j}\omega)| \leq S_u(\omega), \qquad \sup_G |KS(\mathrm{j}\omega)| \leq KS_u(\omega), \\ &\sup_G |GS(\mathrm{j}\omega)| \leq GS_u(\omega)\end{aligned} \tag{17}$$

$$\text{with} \begin{cases} T(s) = \dfrac{G(s)K(s)}{1+G(s)K(s)} & S(s) = \dfrac{1}{1+G(s)K(s)} \\ KS(s) = \dfrac{K(s)}{1+G(s)K(s)} & GS(s) = \dfrac{G(s)}{1+G(s)K(s)} \end{cases} \tag{18}$$

where S_u, T_u and T_l are constraints defined by the designer. It is easy to show that the multiplicative uncertainty $\Delta_m\beta(s)$ of the open-loop frequency response, which defines the frequency-domain uncertainty in the Nichols chart, is invariant and equal to that of the plant:

$$\beta(s) = G(s)K(s) = G_0(s)\Delta_m G(s)C(s) = \beta_0(s)\Delta_m G(s) \tag{19}$$

where $G_0(s)$ and $\beta_0(s)$ are the nominal plant and open-loop transfer functions and where $\Delta_m G(s)$ (or $\Delta_m\beta(s)$) is a multiplicative uncertainty model. Thus, the uncertainty frequency-domains related to the Nichols locus of $\beta_0(\mathrm{j}\omega)$ are defined by all the possible values of the ordered pair

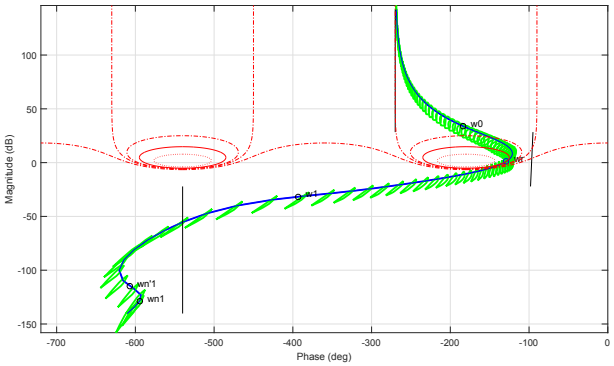

Fig. 9. Open loop Nichols locus for the nominal plant and associated parametric uncertainties

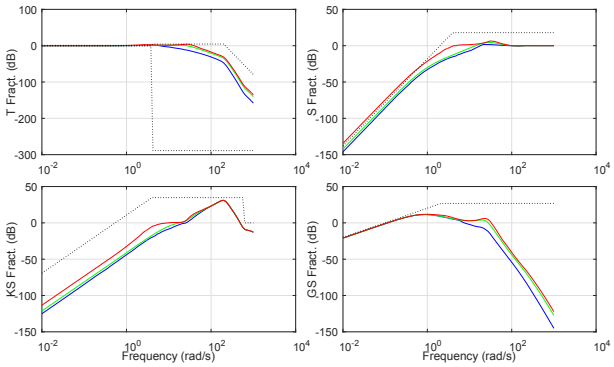

Fig. 10. Sensitivity functions and user defined constraints

$(\arg \Delta_m G(\mathrm{j}\omega), |\Delta_m G(\mathrm{j}\omega)|_{dB})$. By minimizing criterion J (16), the optimal parameters position the uncertainty frequency domains so that they overlap as little as possible the low stability margin areas of the Nichols chart. As the uncertainties are taken into account by the least conservative method, only a nonlinear optimization method can be used.

For $N^- = N^+ = 0$, only four independent open-loop parameters have to be optimized. The parametrization of the open-loop transfer function by complex fractional orders then simplifies the optimization considerably. During optimization, a complex order has the same role as a whole set of parameters used by common rational controllers. Finally, the fractional controller $K_{\mathrm{F}}(s)$ is defined by its frequency response:

$$K_{\mathrm{F}}(\mathrm{j}\omega) = \frac{\beta_0(\mathrm{j}\omega)}{G_0(\mathrm{j}\omega)}. \tag{20}$$

The parameters of a rational (i.e. with integer orders) transfer function $K(s)$ with a predefined low-order structure are tuned to fit the ideal frequency response $K_{\mathrm{F}}(\mathrm{j}\omega)$. Any frequency-domain system-identification technique can be used.

When the controller has to be discrete-time implemented within a processor, it is usual to design it with a continuous time-domain methodology and then to discretize the derivative operator by using a small sampling time. Unfortunately, this leads both to a long processing time and to a bad condition number of the resulting digital controller. To avoid these problems, the initial digital control-system design problem with the sample period T_s can be transformed into a pseudo-continuous problem [10] by:

- taking into account the transfer function of a zero-order hold on the plant input;
- computing the z-transform of the continuous-time set plant and hold;
- achieving a bilinear variable change, for instance $z^{-1} = (1-w)/(1+w)$.

The plant set is characterized by the transfer function $G(w)$, and the optimization of the open loop behaviour defined by (12) in which variable s is replaced by variable w (with $w = \mathrm{j}\nu$), is thus done in the pseudo frequency-domain where the normalized pseudo-frequency is defined by $\nu = \tan(\omega T_s/2)$.

D. CRONE controller design

The current trajectory sampling induces a $(\pm 0.01\,\mathrm{rad})$ noise signal around $600\,\mathrm{rad{\cdot}s^{-1}}$ which imposes some constraints on the loop shaping. The motors also have a control power limitation, as well as a noise n_r induced by the shaft encoder on the rotor. Therefore, the following specifications were imposed :

- a first overshoot of the closed loop step response close to 20% for the nominal plant, leading for a resonance peak of T to the nominal value 1.74 dB ;
- a bandwidth about $\omega_c = 15\,\mathrm{rad{\cdot}s^{-1}}$;
- a control effort sensitivity ($KS(s)$) lower than 0dB around $600\,\mathrm{rad{\cdot}s^{-1}}$ to limit the amplification of the measurement noise induced by the trajectory points.

A low-pass filter (order 2) with a cut-off frequency of $200\,\mathrm{rad{\cdot}s^{-1}}$ and a notch filter (center frequency of $700\,\mathrm{rad{\cdot}s^{-1}}$) were added during the design process, to help meet the control effort constraint. The optimal open loop parameters (of (14) in which variable s is replaced by $w = \mathrm{j}\nu$) obtained using the CRONE toolbox [14] are:

- $C_0 = 26.16$,
- $\omega_0 = 0.8\,\mathrm{rad{\cdot}s^{-1}}$ and $\omega_1 = 180\,\mathrm{rad{\cdot}s^{-1}}$,
- $a_0 = 1.07$, $b_0 = -0.08$ and $q_0 = 1$,
- $\omega_r = 15\,\mathrm{rad{\cdot}s^{-1}}$.

The open loop Nichols locus for the nominal plant and the associated uncertainties are shown in Fig. 9. Constraints on sensitivity functions are shown in Fig. 10 which shows that the optimal open loop behaviour can meet the constraints while ensuring the best stability possible. An order 12 rational controller $K(s)$ has been tuned by using (20).

E. Simulation results

The simulations presented here were made using a $50\,\mathrm{m}$ tether, and a small kite of $16\,\mathrm{m}^2$. The different parameters of the model were based on real measurements [2]. The path-following strategy performs as expected, for every trajectory tested within the wind window. The initial position of the kite was aligned with wind and the transition from its initial position to the desired trajectory is gradual as required. Fig. 11 depicts two simulations where the blue line is the desired trajectory. Trajectory A is a horizontal eight-shaped trajectory centered on the wind, while trajectory B is an vertical trajectory at the edge of the wind window.

The motors still remain a physical limit which can constrain the precision for difficult trajectories that require a high command variation in a short span of time. Even if the kite cannot follow exactly the desired trajectory, the robust controller maintains it within the best possible range, which can be considered enough as the main objective is the generation of traction, and not necessarily a perfect trajectory. Fig. 12 depicts the control effort of the motors, saturated at ± 1000 and Fig. 13 shows the corresponding command δ required to control the kite around both

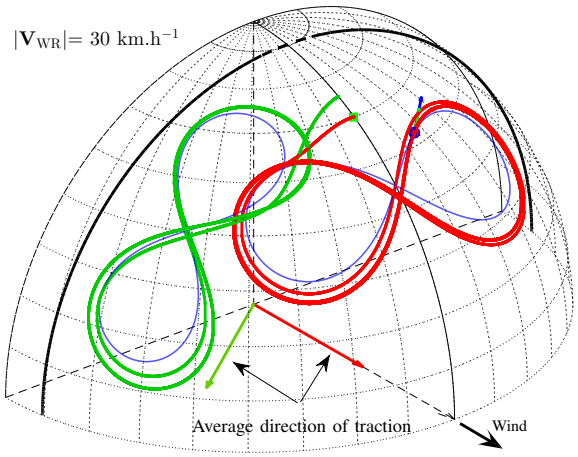

Fig. 11. Simulation representing a horizontal eight-shaped trajectory (Traj A, red) and a vertical eight-shaped trajectory (Traj B, green) for a $30\,\mathrm{km}\cdot\mathrm{h}^{-1}$ wind velocity $|\mathbf{V}_{WR}|$. Both desired trajectory are represented by a dashed blue line.

trajectories.

The theoretical traction generated by the kite on those trajectories can also be deduced from the model and is shown for the two simulations in Fig. 14. The wind speed being identical, the main reason for the difference in traction comes from the position of the trajectory. Trajectory B being at the edge of the wind window, the generated traction is expected to be lower. However, trajectory A is closer to power zone and thus generates more traction. Is is important to note that generating the maximum traction possible is not the only objective of the automatic pilot. While trajectory B produces less power, its generated traction vector is not aligned with the wind, which enables a ship to steer in another direction than the wind.

V. CONCLUSIONS

In this paper, a kite model has been presented that can recreate a coherent kite behaviour within its wind window. A path-following strategy around any eight-shaped path has been described. Based on this groundwork, a closed-loop identification of the kite model was carried out in simulation. Taking the actuators in consideration, the design of a robust controller using a CRONE approach was then explained. The robust controller and path following strategy enables the kite to pursue any eight-shaped trajectory within the wind window, independent of the wind velocity. The simulations also compared the traction generated from both trajectories, which is the most important information for ship propulsion.

The application of this robust controller on a real kite is planned in the near future, using the kite currently available by Beyond The Sea and used for the simulations. The validation of the entire system will lead to assessing its usability on bigger kites and higher altitude, so as to implement them on sailing ships.

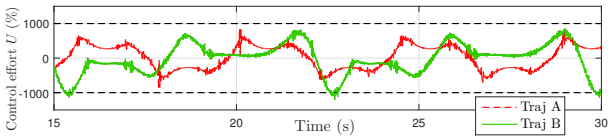

Fig. 12. Control effort U remains between ± 1000 for both trajectories.

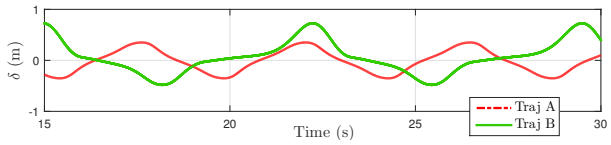

Fig. 13. Asymmetrical command δ needed for the horizontal eight-shaped trajectory and vertical trajectory.

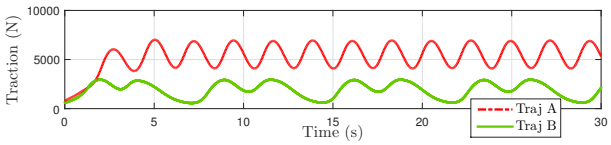

Fig. 14. Traction generated by the kite while following two different trajectories.

REFERENCES

[1] J. Breukels and W. J. Ockels. A multi-body system approach to the simulation of flexible membrane airfoils. *Aerotecnica Missili Spazio 89(3)*, pages 119–134, 2010.

[2] B. Cadalen, J. Sabatier, P. Lanusse, F. Griffon, and Y. Parlier. Modeling and control of a tethered kite in dynamic flight. *Innovsail Conference On Innovation In High Performance Sailing Yachts 4th EDITION*, 2017.

[3] G. M. Dadd, D. A. Hudson, and R. A. Shenoi. Determination of kite forces using three- dimensional flight trajectories for ship propulsion. *Renewable Energy*, vol. 36, 2011.

[4] S. G. De Groot. Modelling the dynamics of an arc-shaped kite for control law design. *Ph. D. Thesis. Delft University of Technology*, 2010.

[5] S. G. De Groot, J. Breukels, R. Schmehl, and W. J. Ockels. Modeling kite flight dynamics using a multibody reduction approach. *Journal of Guidance, Control, and Dynamics*, vol. 34, No. 6, 2011.

[6] A. De Wachter. Power from the skies: Laddermill takes airborne wind energy to newheights. *Leonardo Times: Journal of the Society of Aerospace Engineering Students VSV Leonardo da Vinci*, 2010.

[7] M. Erhard and H. Strauch. Control of towing kites for seagoing vessels. *arXiv*, vol. abs/1202.3641, 2012.

[8] L. Fagiano. Control of tethered airfoils for highaltitude wind energy generation. *Ph. D. Thesis. Royal Turin Polytechnic*, 2009.

[9] U. Fechner, R. Van Der Vlugt, Schreuder E., and R. Schmehl. Dynamic model of a pumping kite power system. *Renewable Energy*, vol. 83:705–716, 2015.

[10] C.H. Houpis. Refined design method for sampled-data control systems: the pseudo-continuous-time (pct) control system design. *Control Theory and Applications, IEE Proceedings D*, 132:69 74, 1995.

[11] C. Jehle and R. Schmehl. Applied tracking control for kite power systems. *Journal of Guidance, Control, and Dynamics*, February 2104.

[12] I.D. Landau, D. Rey, A. Karimi, A. Voda, and A. Franco. A flexible transmission system as a benchmark for robust digital control. *European Journal of Control*, 1, Issue 2:77–96, 1995.

[13] B. Lansdorp, R. Ruiterkamp, and W. J. Ockels. Towards flight testing of remotely controlled surfkites for wind energy generation. *AIAA-2007-6643, AIAA Modelling and Simulation Technologies Conference and Exhibit, Hilton Head, SC, USA*, 20-23 August 2007.

[14] P. Lanusse. Crone control system design, a crone toolbox for matlab. *http://www.ims-bordeaux.fr/CRONE/toolbox*, 2010.

[15] R. Leloup. Modelling approach and numerical tool developments for kite performance assessment and mechanical design; application to vessels auxiliary propulsion. *PhD. Thesis, University of Western Brittany*, 2014.

[16] P. Naaijen and V. Koster. Performance of auxiliary wind propulsion for merchant ships using a kite. *Proceedings of the 2nd International Conference on Marine Research and Transportation, Naples, Italy*, pages 45–53, 2830 June 2007.

[17] A. Oustaloup. "systèmes asservis linéaires d'ordre fractionnaire". *Masson, Paris*, 1983.

[18] A. Oustaloup. "la commande crone". *Hermes Editor, Paris*, 1991.

[19] A. Oustaloup, B. Mathieu, and P. Lanusse. The crone control of resonant plants: application to a flexible transmission. *European Journal of Control*, Vol. 1, n2:113–121, 1995.

[20] A. Oustaloup, J. Sabatier, P. Lanusse, R. Malti, P. Melchior, and X. Moreau. An overview of the crone approach in system analysis, modeling and identification, observation and control. *IFAC Proceedings*, vol. 41 (2), 14254-14265, 2008.

[21] Williams P., Lansdorp B., and Ruiterkamp R. Modeling, simulation, and testing of surf kites for power generation. *AIAA Modelling and Simulation Technologies Conference and Exhibit, Honolulu, Hawaii, USA*, vol. 18-21, 2008.

[22] Y Parlier. *beyondthesea.com*.

[23] J. Sabatier, P. Lanusse, P. Melchior, and A. Oustaloup. Fractional order differentiation and robust control design: Crone, h-infinity and motion control. *Intelligent Systems, Control and Automation: Science and Engineering*, vol. 77, Springer 2015.

[24] M. Schlaak, R. Kreutzer, and R. Elsner. Simulating possible savings of the skysails- system on international merchant ship fleets. *International Journal of Maritime Engineering*, vol. 151:25–37, 2009.